Supporting Information

Boronization-induced amorphous-crystalline interface on Prussian blue analogue for efficient and stable seawater splitting

Yikang Wang,[a] Dongmei Jia,[a] Wenyao Zhang,[a] Gan Jia,*[a] Haijiao Xie,[b] Wei Ye,[a] Genping Zhu[a] and Peng Gao*[a]

[a] College of Material, Chemistry and Chemical Engineering, Key Laboratory of Organosilicon Chemistry and Material Technology, Ministry of Education, Hangzhou Normal University, Hangzhou, 311121, China

Gan Jia: gjia@hznu.edu.cn;

Peng Gao: gaopeng@hznu.edu.cn

[b] Hangzhou Yanqu Information Technology Co., Ltd., Hangzhou 310003, People's Republic of China

Experimental Section

Synthesis of Co(OH)F precursor. A piece of commercial nickel foam (NF) was repeatedly cleaned by 3 M HCl solution, acetone, ethanol and deionized water in sequence and dried in the vacuum. The Co(OH)F precursor was synthesized *via* a hydrothermal method. Typically, NH_4F (10 mmol), urea (25 mmol), and $Co(NO_3)_2 \cdot 6H_2O$ (5 mmol) were dissolved into 35 mL deionized water under magnetic stirring. The resulting solution was transferred to a Teflon autoclave containing a piece of cleaned Ni foam (1 cm × 4 cm). and the sealed autoclave was kept at 120 °C for 6 h. The resultant product was taken out and rinsed with ultrapure water for several times.

Synthesis of PBA/NF. The as-obtained Co(OH)F precursor was directly immersed in 25 mL of potassium ferricyanide solution (30 mM) at 50 ℃ for 48 h. After the reaction finished, the sample was rinsed with ultrapure water, followed by drying at 50 ℃.

Synthesis of PBA/NF-*t*. To synthesize boron-modified PBA/NF-*t*, the as-prepared PBA/NF was soaked in $NaBH_4$ solution (0.4 M) containing 0.08 M NaOH at room temperature for 1 h, 2 h, 4 h and 8 h, respectively. After this boron-modification procedure, the PBA/NF-*t* sample was removed from the solution and then dried at 50 ℃.

Materials Characterization. The morphology and nanostructure of the electrocatalysts were examined by scanning electron microscopy (SEM, ZEISS SUPRA 55) and transmission electron microscopy (TEM, FEI TECNAI G20) coupled with energy dispersive X-ray spectroscopy (EDS). Structural and chemical analyses of the as-prepared samples were identified by powder X-ray diffraction (XRD, Cu Kα radiation, Bruker D8 Advance, Germany) and X-ray photoelectron spectroscopy (XPS, Thermo Fisher Scientific, UK). Electron paramagnetic resonance (EPR) spectra were recorded on a Bruker A300 spectrometer. Fourier transform infrared (FT-IR) spectra were recorded with KBr pellets on FT-IR spectrometer (Perkin Elmer, USA). The *ex-situ* Raman spectroscopy was performed with a confocal Raman microscope LabRAM HREvolution (HORIBA Scientific), and the *in-situ* Raman measurement was conducted on an integrated Raman spectroelectrochemical instrument (SPELEC RAMAN, Metrohm AG, Switzerland).

Electrochemical Characterization. Electrochemical characterizations of the as-prepared electrodes were conducted at room temperature on a CHI 660E electrochemical station. The electrochemical tests were accomplished using a two-compartment electrocatalytic cell. A Pt mesh and a Hg/HgO electrode served as the counter electrode and the reference electrode, respectively. The polarization curve of each catalyst was recorded at a scan rate of 5 mV s^{-1} with *iR* compensation after running at least 100 cyclic voltammetry (CV) cycles for activation and stabilization. The potential ($E_{Hg/HgO}$) was calibrated to the reversible hydrogen electrode (RHE) using the equation: $E_{RHE} = E_{Hg/HgO} + 0.098 + 0.059 \times pH$ and the overpotential (η) was calculated by: $\eta(V) = E_{RHE}$ - 1.23 V. The Tafel slope (b) was calculated by $\eta = a + b \log(j)$, in which j is the current density. Electrochemical impedance spectroscopy (EIS) was performed from 100 kHz to 0.01 Hz. To evaluate the electrochemically active surface area (ECSA), CV cycling was performed in the potential range from 0.724 to 0.824 V *vs.* RHE with scan rates ranging from 20 to 140 mV s^{-1}. By plotting the capacitive current at 0.78 V *vs.* RHE against the scan rates, the double-layer capacitance (C_{dl}) was obtained as half of the corresponding slope, and then the ECSA was derived from the equation: ECSA = C_{dl}/C_s, in which C_s is the specific capacitance for a flat surface (40 μF cm^{-2}).

DFT calculation details. The first principle calculations are performed by using the Vienna ab initio simulation package.[S1,S2] The program has the projected enhancement wave pseudopotential[S3] and the generalized gradient approximation of Perdew, Burke and Enzzerhof (PBE) exchange correlation functional,[S4] which is used to optimize the structure and obtain the free energy of all structures. The cutoff energy of the plane waves basis set is 500 eV and a Monkhorst-Pack mesh of 3×3×1 is used in K-sampling in the adsorption energy calculation. U (Co 3d) value of 3.5 eV and U (Fe 3d) value of 3.5 eV were applied to the Co 3d and Fe 3d states.[S5,S6] In addition, van der Waals interactions corrected using DFT-D2 are considered.[S7] The electronic self-consistent iteration is set to 10^{-5} eV, and the positions of all of the atoms are fully relaxed until the residual force on each atom is below 0.02 eV $Å^{-1}$. 15 Å of vacuum layer along the

z-direction is applied to avoid periodic interactions. The free energy of structure A (GA) is calculated by GA = EA + ZPE - TS: the total energy (EA), zero-point energy (ZPE), T is the temperature (298.15K), and the entropy (S) of structure A.

Fig. S1 Natural seawater is collected from the Yellow Sea, China.

Natural seawater was collected from the Yellow Sea, China. Before use in electrochemical tests, the natural seawater was kept in a bottle for more than 24 h to let most of the particles visible to the naked eye settle to the bottom, after which the supernatant was collected.

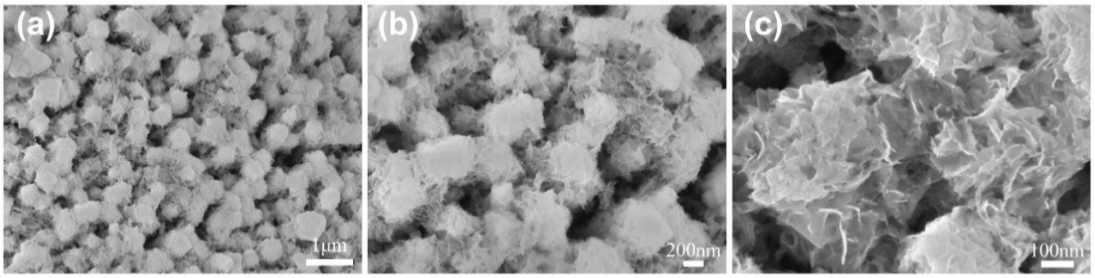

Fig. S2. (a-c) SEM images of PBA/NF-8h.

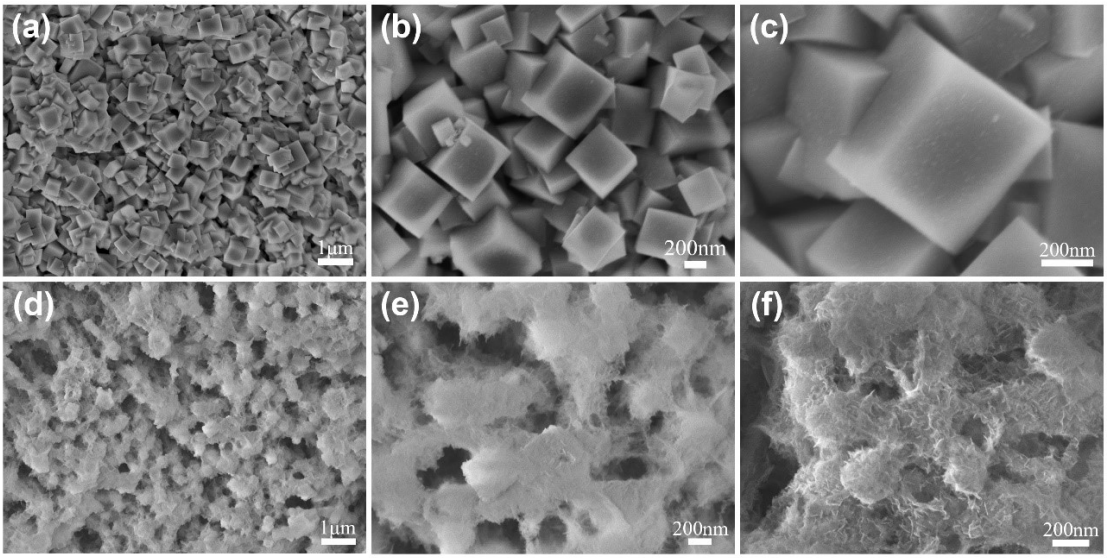

Fig. S3. SEM images of (a-c) PBA/NF-2h (0 ℃) and (d-f) PBA/NF-2h (40 ℃).

When the post-treatment time was further prolonged to 8 h, a large number of nanosheets appeared on the surface, and the structure of PBA frameworks almost collapsed (Fig. S2). In order to explore the effect of temperature on the post-treatment process, the reaction was also carried out in water bath at 0 ℃ and 40 ℃, respectively. After 2 hours of reaction at 0 ℃ (Fig. S3 a-c), the surface of the reaction was smooth, and the existence of nanosheets was rarely observed. During the reaction, there were almost no bubbles in the solution, indicating that the reaction was slow or almost did not occur at lower temperature. However, at 40 ℃ (Fig. S3 d-e), the number of the surface nanosheets was significantly more than that at room temperature after 2 h, but the agglomeration of the nanosheets was more serious, which reduced the exposed active surface.

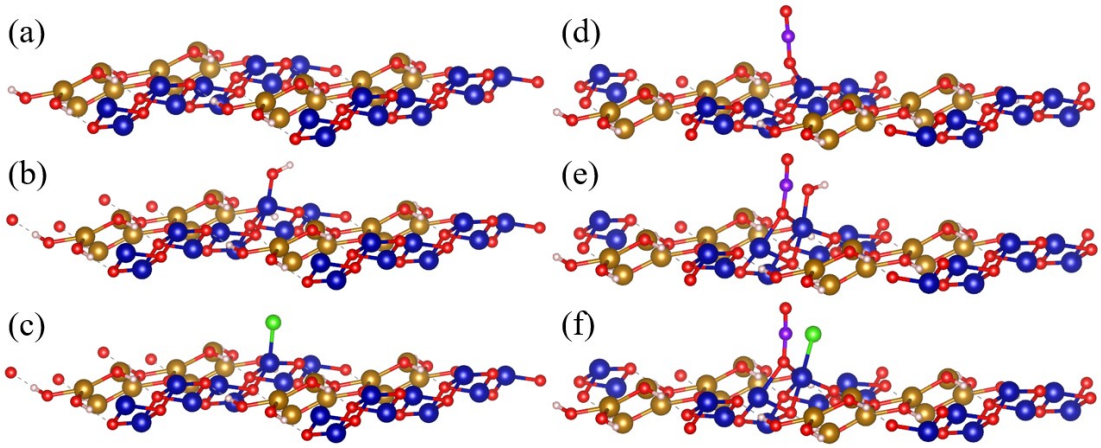

Figure S4. The structure models of (a) (Co, Fe)OOH and (d) BO_2-(Co, Fe)OOH; Optimized structures after adsorption of OH^- and Cl^- on (b, c) (Co, Fe)OOH and (e, f) BO_2-(Co, Fe)OOH, respectively. Color: blue for Co, brown for Fe, red for O, pink for H, green for Cl and purple for boron

To gain further insight into the role of the surface boron-rich layer in electrocatalytic seawater splitting, referring to the previous report[S8], density functional theory (DFT) calculations were carried out by constructing two catalyst surface structural models, (Co, Fe)OOH and BO_2-modified (Co, Fe)OOH (Figure S4). It has been generally accepted that CoFe oxyhydroxides will be *in situ* reconstructed on the surface of CoFe-based OER pre-catalysts and serve as the real active phases. The adsorption energies of OH^- and Cl^- were used to assess the OER electrocatalytic activity and corrosion resistance of the materials in seawater.

As summarized in Figure S5, the adsorption energy of (Co, Fe)OOH for OH^- was -0.67 eV and that for Cl^- was -0.72 eV, after BO_2 modification, the adsorption energy of OH^- is -1.36 eV and that of Cl^- is -0.44 eV, which indicated that the adsorption of OH^- was enhanced while the adsorption of Cl^- was partially suppressed. Besides, the charge density difference maps of both structures are present in Figure S6, which indicating that the boron-rich surface structure facilitates OH adsorption and enables electron transfer to OH.

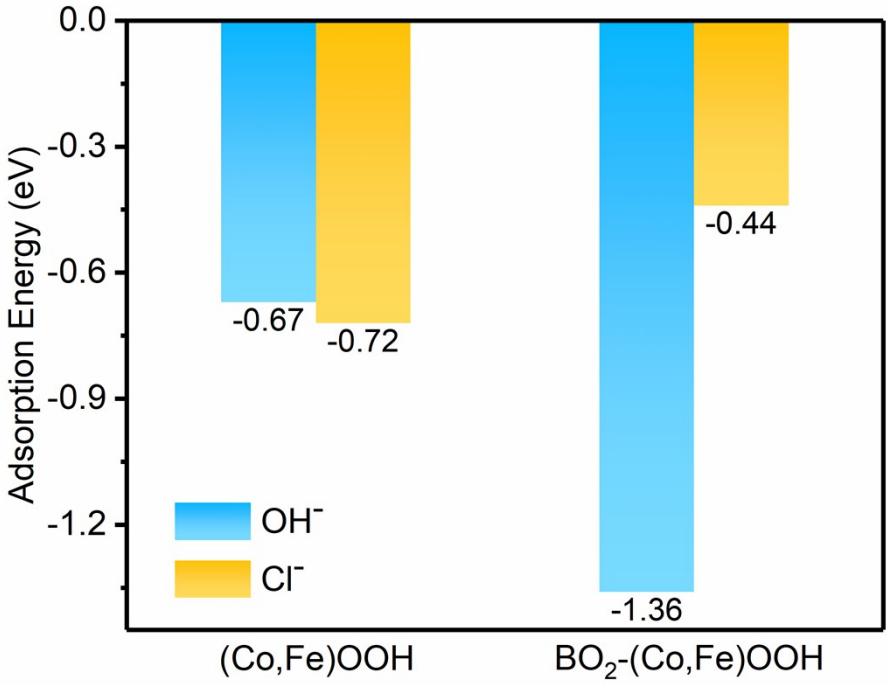

Figure S5. Adsorption energies of OH^- and Cl^-

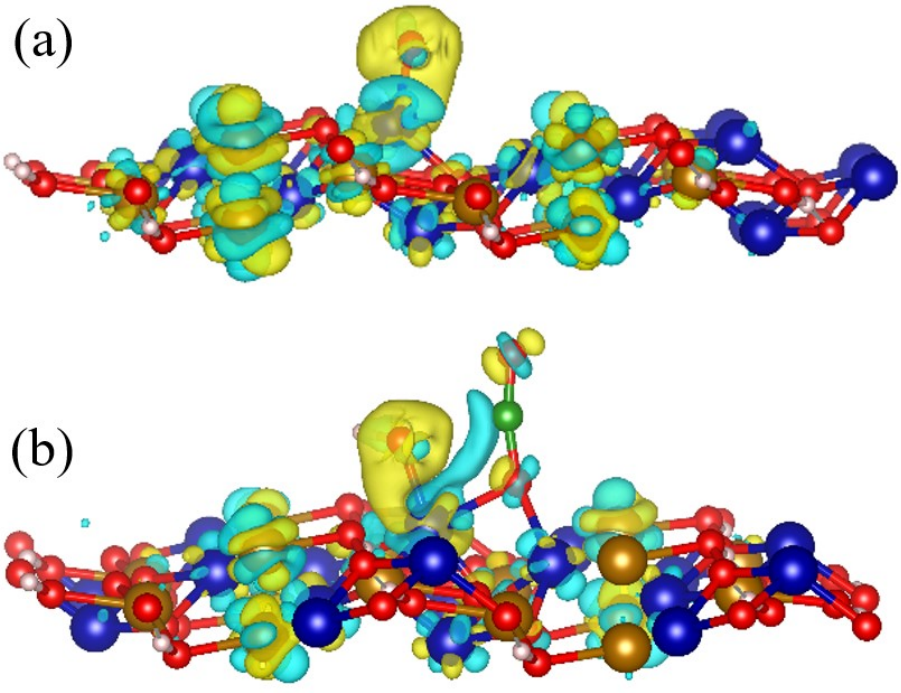

Figure S6. The charge density difference map for both structures.

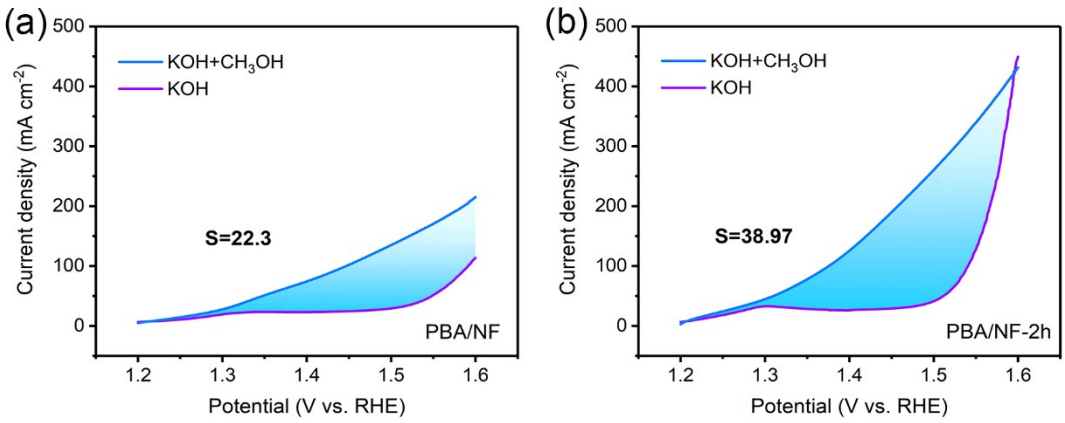

Figure S7. Probing OH* with the electrocatalysts in OER

Among the widely accepted reaction mechanisms, OH* is recognized as the first intermediate in the catalytic cycle of OER, and its binding energies correlate with those of other oxygen intermediates such as O* and OOH*. Previous studies have demonstrated that reactive OH* generated in OER on electrode surface can be probed by the alcohol oxidation reaction. This is because the OH* intermediate is an electrophile and can be probed by reacting with a nucleophile such as methanol molecule.[S9,S10] In consequence, the LSV curves were collected in 1 M KOH and 1 M KOH + CH_3OH electrolyte. The discrepancy in current brought by methanol oxidation can reflect the surface coverage of OH*, which further feedbacks the adsorption capacity of OH*.

Calculate the filled area ($S_{PBA/NF}$ = 22.3, $S_{PBA/NF-2h}$ = 38.97) between the LSV curves to quantify the difference in current during the reaction (Figure S7). It can be shown that the amorphous-crystalline structure after $NaBH_4$ treatment increases the adsorption of OH*.

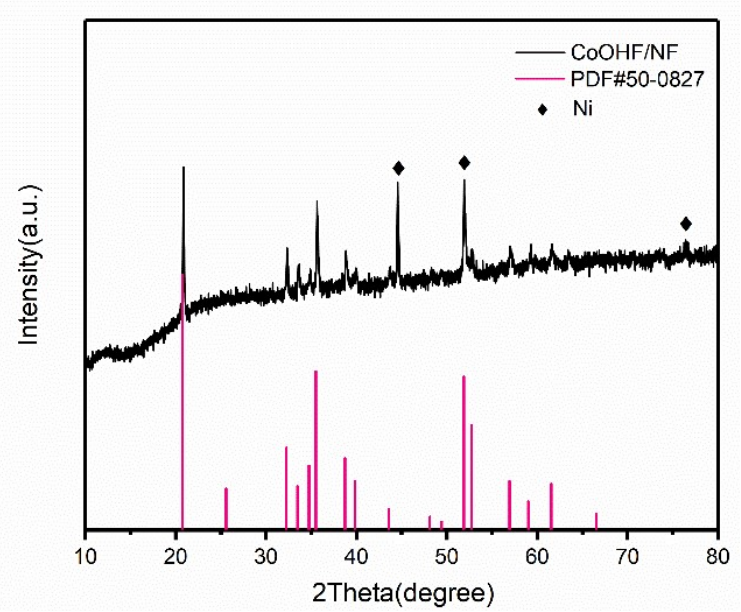

Fig. S8. XRD pattern of Co(OH)F precursor.

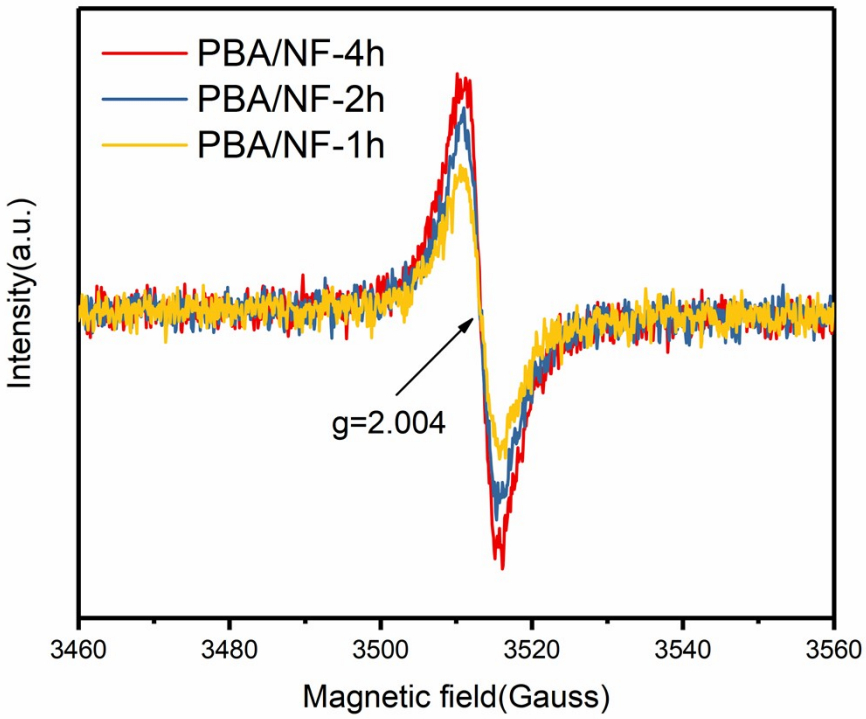

Fig. S9. EPR spectra of PBA/NF-1h, PBA/NF-2h and PBA/NF-4h

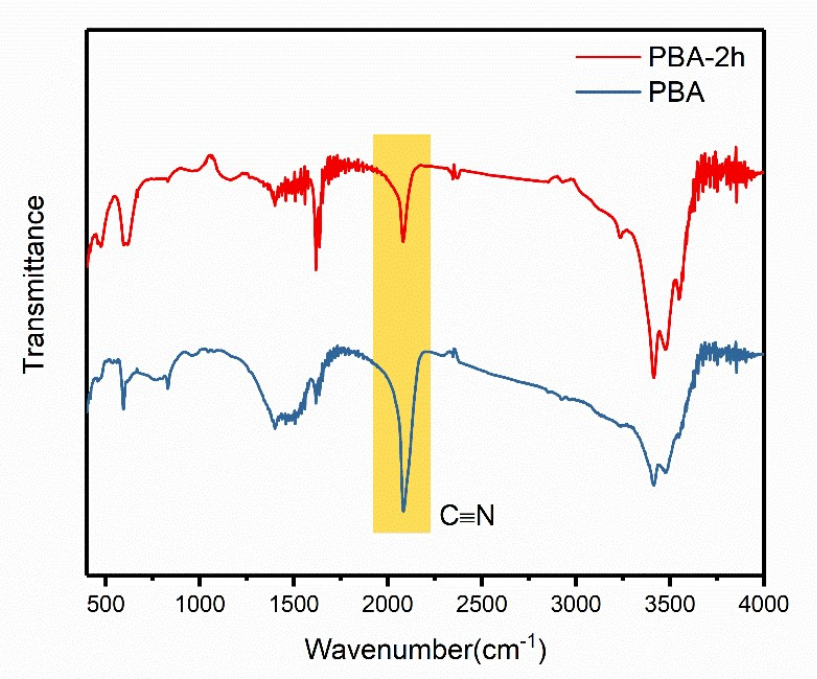

Fig. S10. FTIR spectra of pristine PBA/NF and PBA/NF-2h.

As shown in Fig. S10, the stretching vibration of *v*(OH) and bending vibration bond of *δ*(OH) of coordinated water molecules on PBA framework can be observed around 3414 cm^{-1} and 1617 cm^{-1}, respectively.[S11] The characteristic peak at 2082 cm^{-1} can be attributed to the vibration of CN moiety in PBA.[S12]

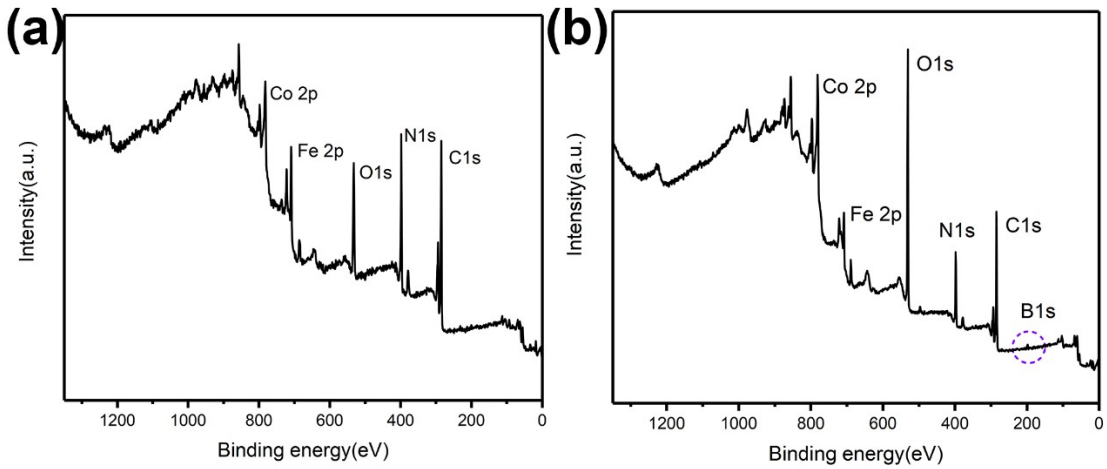

Fig. S11. XPS survey spectra of PBA/NF and PBA/NF-2h.

As shown in Figure S11, XPS spectra show that PBA/NF contains Co, Fe and O elements, while PBA/NF-2h contains Co, Fe, O and B elements.

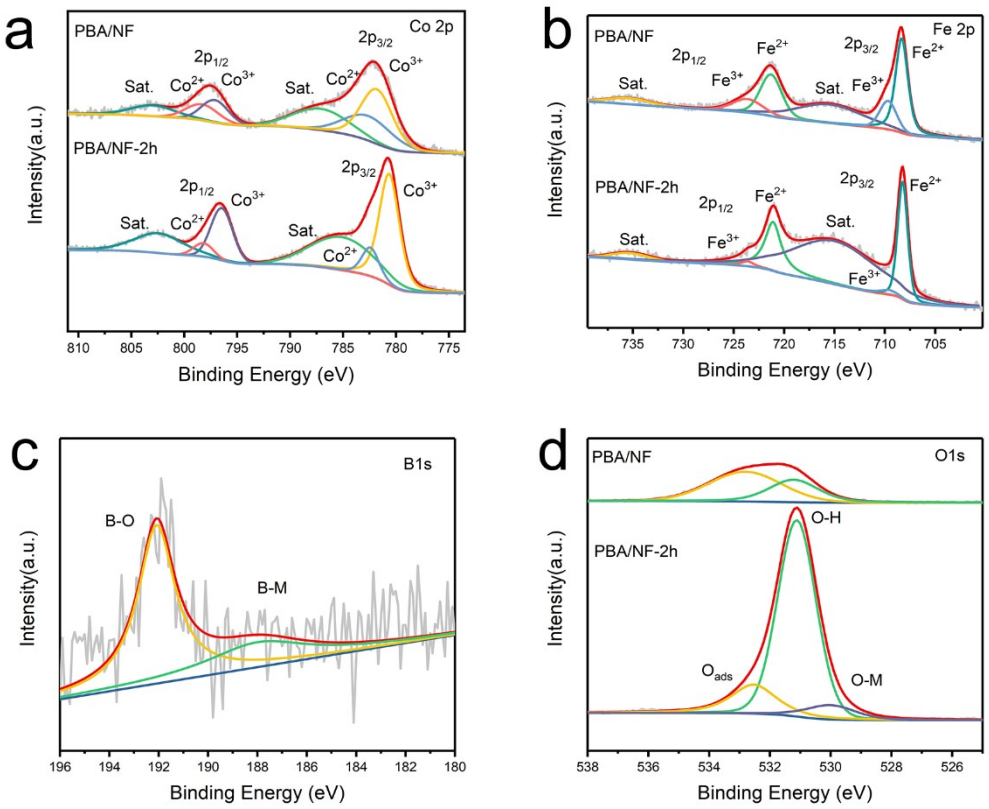

Fig. S12. High-resolution XPS spectra for PBA/NF and PBA/NF-2h in the (a) Co 2p, (b) Fe 2p, (c) B 1s and (d) O 1s.

Although the preparation of CoFe-PBA is derived from Fe (III) cyanide and Co (II) salt, electron transfer occurs simultaneously in the PBA skeleton, from the anti-bonding e_g* orbital of Co(II) to the bonding t_{2g} orbital of Fe(III), the stability energy of ligand field can be maximized. Therefore, the majority of metal valence states in the original CoFe-PBA are Fe (II) and Co(III).

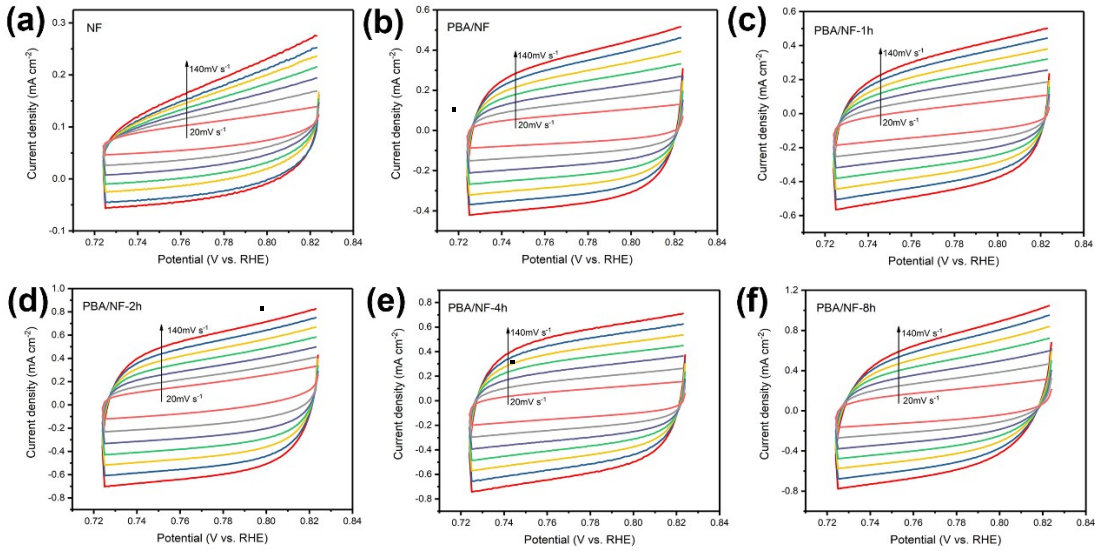

Fig. S13. CV curves for calculation of double-layer capacitance. CV curves of (a)NF, (b) PBA/NF, (c) PBA/NF-1h, (d) PBA/NF-2h, (e) PBA/NF-4h and (f) PBA/NF-8h at scan rates ranging from 20 mV s^{-1} to 140 mV s^{-1} with an interval of 20 mV s^{-1}.

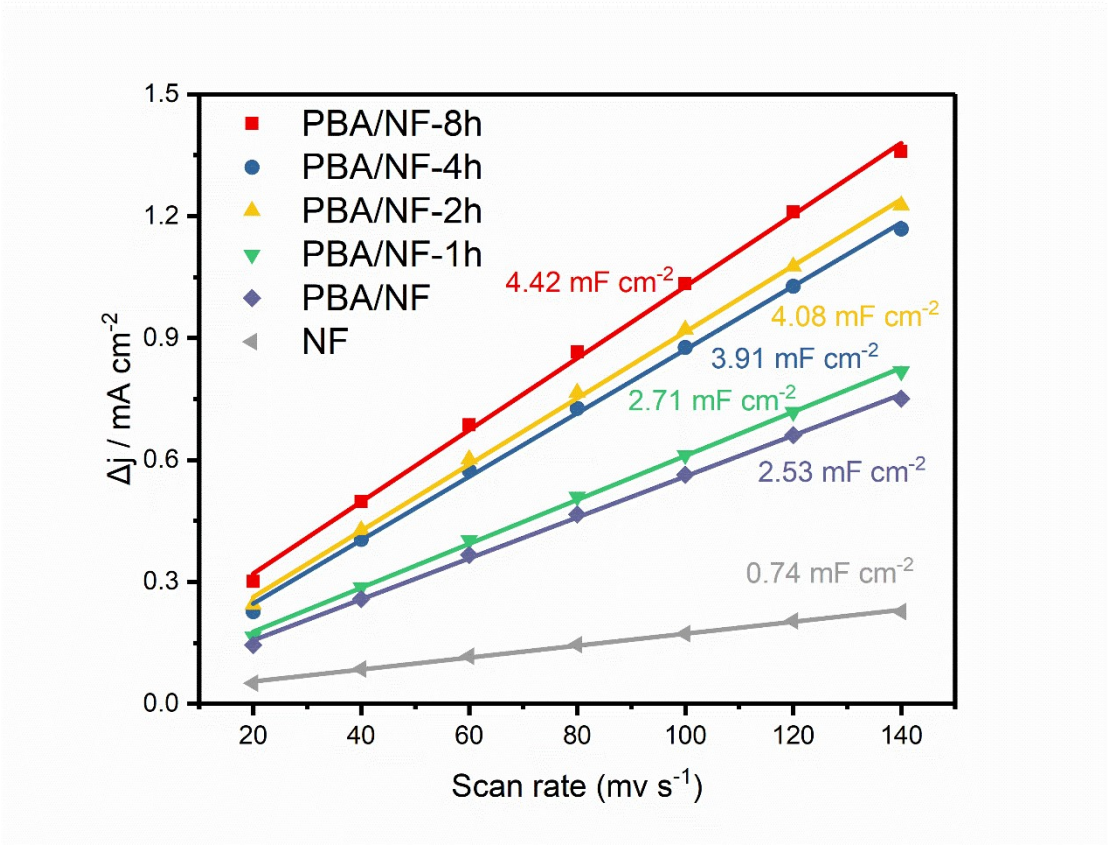

Fig. S14. The double-layer capacitance (C_{dl}) image.

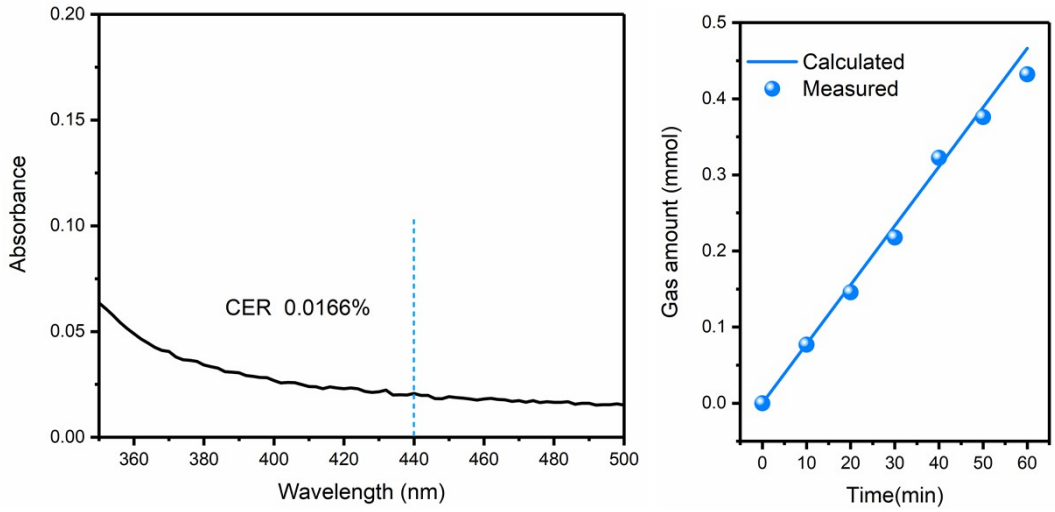

Fig. S15. (left) Visible spectra of the electrolytes with KI taken after electrolysis with the indicated delivered charges at a constant current of 200 mA cm^{-2} on PBA/NF-2h electrode; (right) Collected (dots) and theoretical (solid line) gaseous products (O_2) at a constant density in alkaline simulated seawater.

Cl_2 has a large solubility in water (3.26 g L^{-1} at 25 °C) and can react with water to form hypochlorite ion (ClO^-) (eq1).[S13] When KI is added, the generated ClO^- reacts with I^- to produce I_2 by the quantitative redox process (eq2).

$$Cl_2 + 2OH^- \rightarrow ClO^- + Cl^- + H_2O \quad (1)$$

$$ClO^- + 2I^- + H_2O \rightarrow I_2 + 2Cl^- + 2OH^- \quad (2)$$

The absorption spectrum was used to determine the concentration of I_2.[S13, S14] Electrolysis was performed on PBA/NF-2h in 1 M KOH and 0.5 M NaCl solution at a constant current density of 200 mA cm^{-2} for 1 h. Afterward, a portion of the electrolyte was extracted and then added with KI to assess the I_2 concentration (Figure S15). The I_2 will then show an absorption peak around 440 nm.[S15] The Faradaic efficiency of the ClER was evaluated as follows (eq 3),

$$\varepsilon_{CER}\,(\%) = [Cl_2]V/\{Q/(n \times F)\} \times 100 \quad (3)$$

where V represents the electrolyte volume, Q is the accumulated charge during electrolysis, F is the faradaic constant (96485 C mol^{-1}), and n represents the number of transferred electrons. The intensity of absorption peak at 440 nm was negligible, which indicates that the oxidation of Cl^- to OCl^- was vastly suppressed on PBA/NF-2h.

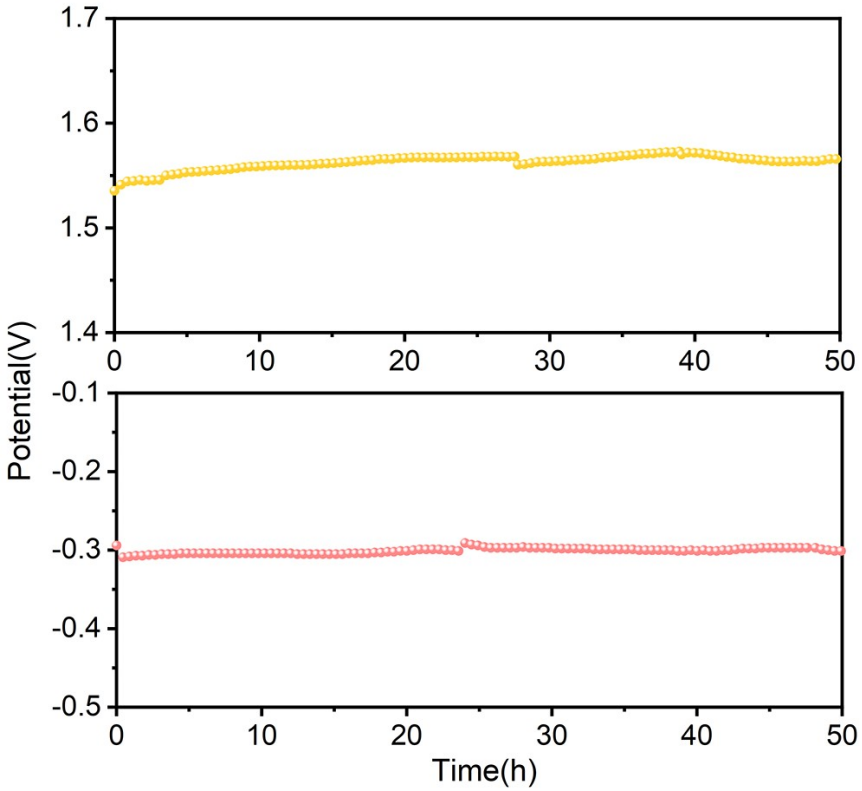

Fig. S16. Chronopotentiometric curves of PBA/NF-2h in alkaline seawater electrolytes. (50 mA cm^{-2} for OER and 100 mA cm^{-2} for HER)

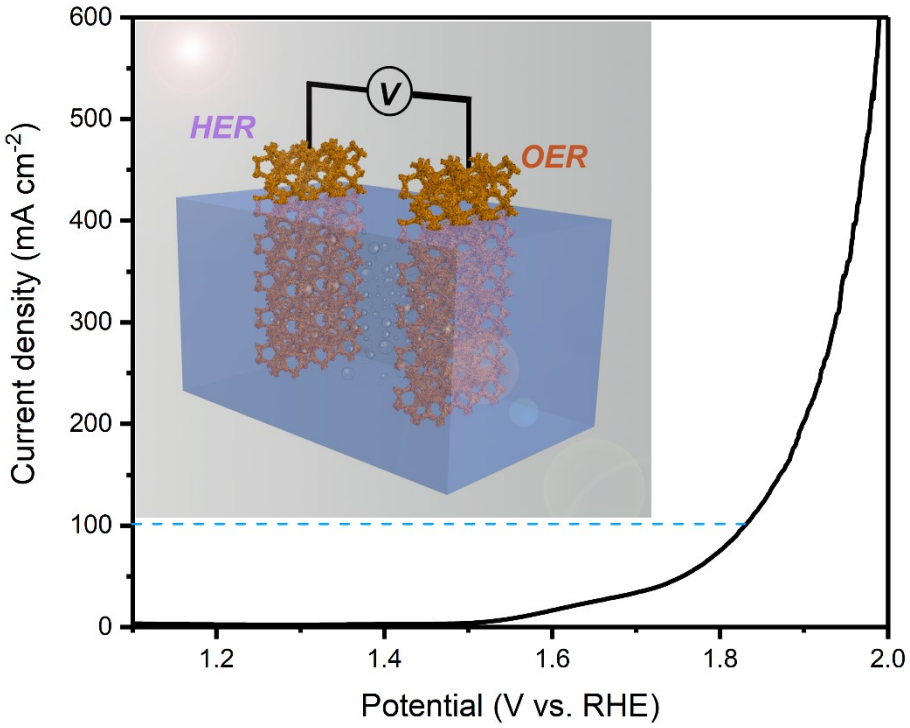

Fig. S17. Polarization curves of PBA/NF-2h catalyst in a two-electrode electrolyzer tested in alkaline simulated (1 M KOH + 0.5 M NaCl) seawater electrolytes.

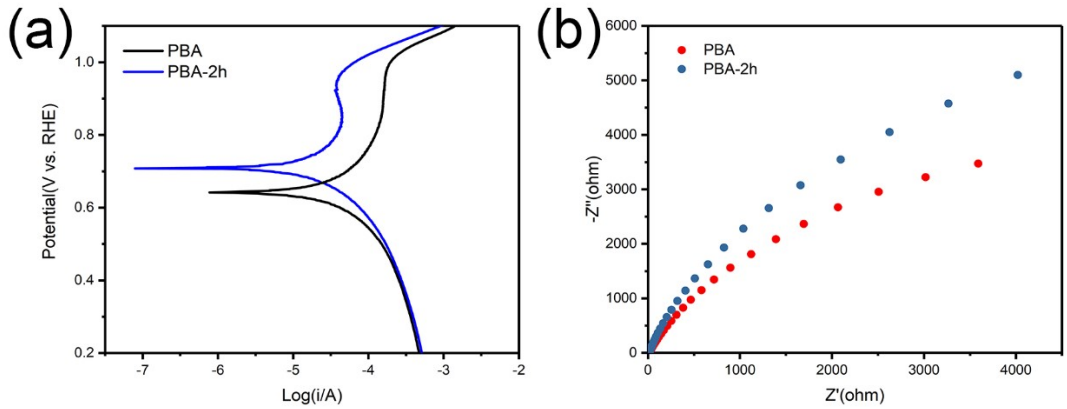

Fig. S18. (a) Potentiodynamic polarization curves for PBA/NF and PBA/NF-2h. (b) The Nyquist plots for PBA/NF and PBA/NF-2h in 1 M KOH + 0.5 M NaCl solution.

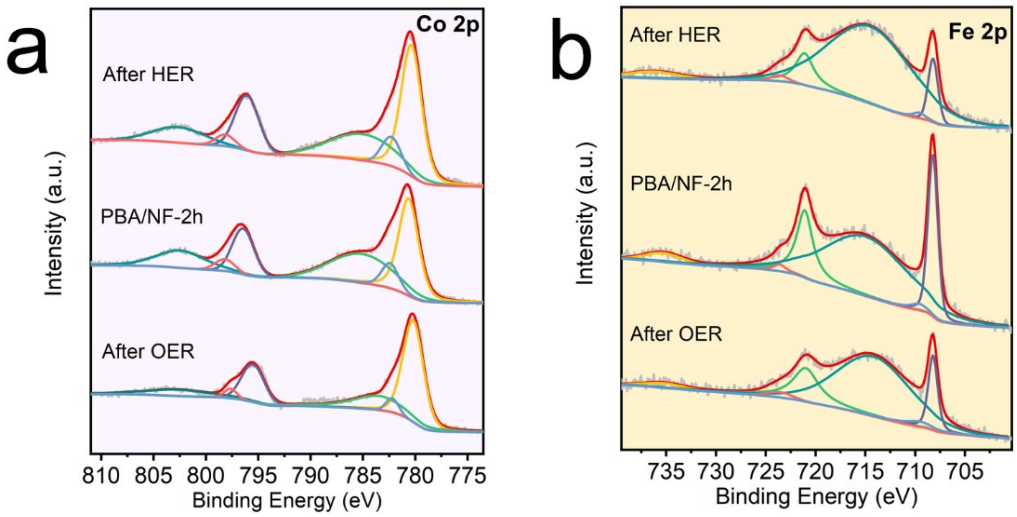

Fig. S19. Characterization after electrocatalytic HER and OER tests: a) Co 2p and b) Fe 2p XPS spectra

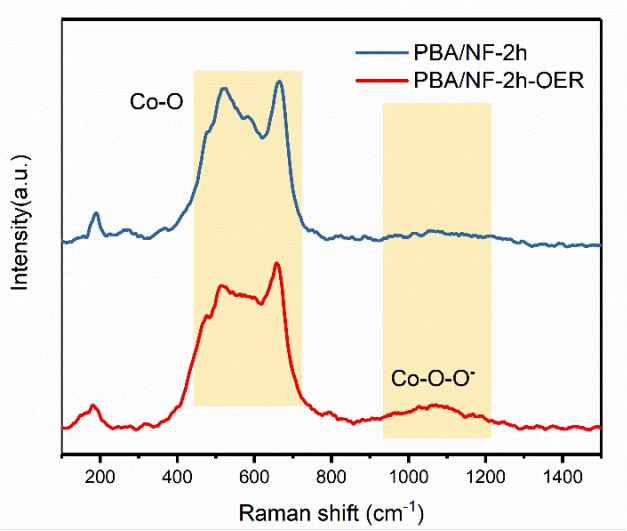

Figure R13. *Ex situ* Raman spectra of PBA/NF-2h before and after OER chronoamperometry

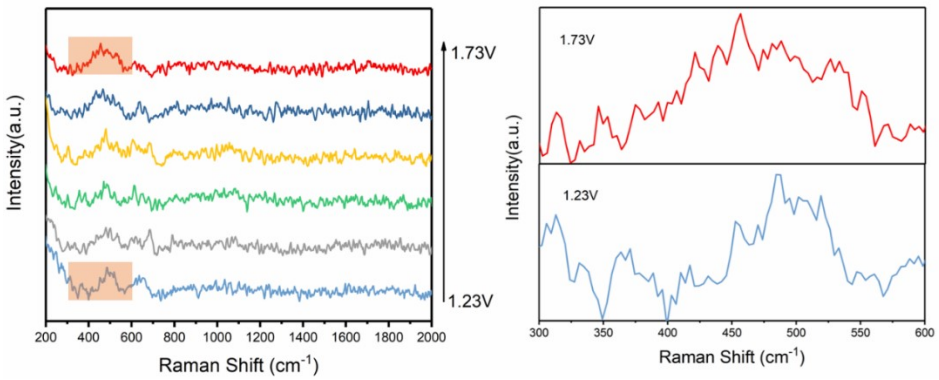

Figure R14. *In situ* electrochemical Raman spectra of PBA/NF-2h under different applied potentials.

Raman spectroscopy was used to determine the active species in the OER process (Figure R13). The peaks centered at ~ 532 and 665 cm^{-1} in Raman spectra are assigned to E_g and A_{1g} vibrational modes of Co-O, respectively. After the OER test, a broad vibrational band at 1072 cm^{-1} lies in the range reported for the stretching modes of superoxide species (1000–1200 cm^{-1}). The superoxide species ($CoOO^-$) are deemed as an active intermediate in the OER.[S16] From 1.23 to 1.73 V, the *in-situ* Raman peaks (Figure R14) corresponding to the stretching vibration of Co-O at 486 cm^{-1} shift to a lower frequency, which is related to the change of bond length of the Co-O bond.[S17, S18] The above-mentioned results indicated that Co is the main adsorption site for the reaction.

References

S1. G. Kresse and J. Furthmüller, Comp. Mater. Sci., 1996, 6, 15-50.

S2. M. D. Segall, P. J. D. Lindan, M. J. Probert, C. J. Pickard, P. J. Hasnip, S. J. Clark and M.C. Payne, J. Phys. Condens. Matter, 2002, 14, 2717-2744.

S3. P. E. Blochl, Phys. Rev. B, 1994, 50, 17953-17979

S4. J. P. Perdew, K. Burke and M. Ernzerhof, Phys. Rev. Lett., 1996, 77, 3865-3868.

S5. A. Tilocca and A. Selloni, J. Phys. Chem. C 2012, 116, 9114−9121.

S6. M. García-Mota, A. Vojvodic, F. Abild-Pedersen and J. K. Nørskov, J. Phys. Chem. C 2013, 117, 460−465.

S7. S. Grimme, J. Comput. Chem., 2006, 27, 1787-1799

S8. J. Li, Y. Liu, H. Chen, Z. Zhang and X. Zou, Adv. Funct. Mater., 2021, 31, 2101820.

S9. H. B. Tao, Y. Xu, X. Huang, J. Chen, L. Pei, J. Zhang, J. G. Chen and B. Liu, Joule, 2019, 3, 1498-1509.

S10. H Chen, J Chen, P Ning, X Chen, J Liang, X Yao, D. Chen, L. Qin, Y. Huang and Z. Wen, ACS Nano 2021, 15, 12418-12428.

S11. Q. Wang, S. He, N. Wang, J. Zhao, J. Fang and W. Shen, New J. Chem., 2016, 40, 3244-3251.

S12. D. Li, C. Zhou, Y. Xing, X. Shi, W. Ma, L. Li, D. Jiang and W. Shi, Chem. Commun., 2021, 57, 8158-8161.

S13. H. Abe, A. Murakami, S. Tsunekawa, T. Okada, T. Wakabayashi, M. Yoshida and M. Nakayama, ACS Catal., 2021, 11, 6390-6397.

S14. T. Okada, H. Abe, A. Murakami, T. Shimizu, K. Fujii, T. Wakabayashi and M. Nakayama, Langmuir, 2020, 36, 5227-5235.

S15. H. Goto, Polymers, 2011, 3, 875-885.

S16. A. Moysiadou, S. Lee, C. S. Hsu, H. M. Chen and X. Hu, J. Am. Chem. Soc. 2020, 142, 11901-11914.

S17. L. Tang, L. Yu, C. Ma, Y. Song, Y. Tu, Y. Zhang, X. Bo and D. Deng, J. Mater. Chem. A, 2022, 10, 6242-6250.

S18. S. Lee, A. Moysiadou, Y. C. Chu, H. M. Chen and X. Hu, Energy Environ. Sci., 2022, 15, 206-214.